Millimeter-wave interferometry and far-forward scattering for density fluctuation measurements on LTX-β[a)]

S. Kubota,[1, b)] R. Majeski,[2] D. P. Boyle,[2] R. Kaita,[2] T. Kozub,[2] R. Lantsov,[1] E. Merino,[2] X. V. Nguyen,[1] W. A. Peebles,[1] and T. L. Rhodes[1]

[1)]*Department of Physics and Astronomy, University of California, Los Angeles, CA 90095*

[2)]*Princeton Plasma Physics Laboratory, Princeton, NJ 08543*

The $\lambda \approx 1$ mm ($f=288$ GHz) interferometer for the Lithium Tokamak Experiment-β (LTX-β) will use a chirped-frequency source and a centerstack-mounted retro-reflector mirror to provide electron line density measurements along a single radial chord at the midplane. The interferometer is unique in the use of a single source (narrow-band chirped-frequency interferometry) and a single beamsplitter for separating and recombining the probe and reference beams. The current work provides a documentation of the interferometry hardware and evaluates the capabilities of the system as a far-forward collective scattering diagnostic. As such, the current optical setup is estimated to have a detection range of $0.4 \lesssim k_\perp \lesssim 1.7$ cm^{-1}, while an improved layout will extend the upper $k_\perp$ limit to ~ 3 cm^{-1}. Measurements with the diagnostic on LTX are presented, showing interferometry results and scattered signal data. These diagnostics are expected to provide routine measurements on LTX-β for high frequency coherent density oscillations (e.g., Alfvénic modes during neutral beam injection) as well as for broadband turbulence.

I. INTRODUCTION

UCLA has operated a set of microwave and millimeter-wave diagnostics for electron density measurements on the Lithium Tokamak Experiment (LTX).[1,2] An FM-CW (frequency-modulated continuous-wave) reflectometer[3] (13.1−33.5 GHz) has provided density profiles with high spatial (< 0.5 cm) and temporal resolution (8 μs), while a millimeter-wave ($f = 288$ GHz or $\lambda \approx 1$ mm) interferometer has measured line-averaged densities with a 1.33 μs time resolution. LTX-β[2] is an upgrade to the device, which will double the toroidal field (from 1.7 to 3.4 kG) and the plasma current (from 85 to 150−175 kA), and also have neutral beam injection. The interferometer is part of a diagnostic package that aims to detect electron density fluctuations across a broad wavenumber range. The FM-CW reflectometer will be used to measure radial backscattering from fluctuations with $k_r \lesssim 14$ cm^{-1}, while a dual-channel tunable-frequency reflectometer (13.5−20.5, 27−40 GHz) will detect oscillations with $k_\perp \lesssim 1$ cm^{-1}. Here k_r and $k_\perp$ represent the radial and perpendicular wavenumbers, respectively, for fluctuations along a radial beam path located on the midplane of the device. The degree of access across the major radius of the plasma will be dictated by the magnetic fields and electron density profiles attained in LTX-β.

The operation of the interferometer as a far-forward collective scattering[5–7] diagnostic is a simple way to provide additional fluctuation measurements across a wide variety of discharges, since the hardware for the two measurement methods can be identical. Far-forward scattering (FFS) is a diagnostic technique for measuring low-$k_\perp$ electron density fluctuations, where the scattered portion of the probe beam lies close to or within the divergence angle of the main beam (i.e., $\theta_s \lesssim \theta_{div}$). The scattering angle θ_s obeys the Bragg rule $k_\perp = 2k_p \sin(\theta_s/2)$, where k_p is the wavenumber of the probing wave. In interferometry, the phase of the intermediate frequency (IF) signal provides information about density fluctuations in a line-integrated sense, with the wavenumber response proportional to $\exp(-k_\perp^2 w^2/4)$ (w is the beam radius) that is centered at $k_\perp = 0$. In FFS, the scattered beam will have a direction that is offset from the main beam by angle θ_s, and a phase that is modulated by the oscillation of the perturbation. Hence a detector, collecting both the main beam and the scattered wave, will generate an IF signal that exhibits an amplitude modulation having a modulation index that is proportional to the density fluctuation level, and a time dependence that is equal to the frequency of the perturbation. The wavenumber response of the amplitude modulation is estimated using a Fourier optics approach[6] is proportional to $k_\perp^2 w^2 \exp(-k_\perp^2 w^2/8)$, which has a maximum at $k_\perp w = 2\sqrt{2}$ (offset from $k_\perp = 0$). This value for $k_\perp$ is equivalent to setting $\theta_s(= k_\perp/k_p = 2/k_p w_0) = \theta_{div}$, if we make the assumption that the scattering region is located at the Rayleigh range of the beam (where $w = \sqrt{2}w_0$ and w_0 is the radius at the beam waist). Enhanced contrast for both coherent fluctuations and low-k turbulence using FFS has been reported on a number of devices[8–11].

This article provides a description of the interferometry hardware and evaluates the performance of the optical setup for FFS measurements. Section II of this article describes the plasma device and the various components of the diagnostic. Section III compares two optical setups for FFS measurements: 1) the current beam transmission line and 2) a design that reduces beam truncation due to the finite size of the optical components. Section IV presents previous interferometry measurements on LTX, and discusses contributions to the IF signal from FFS. Section V summarizes this article and presents future directions for the development of the hardware as a far-
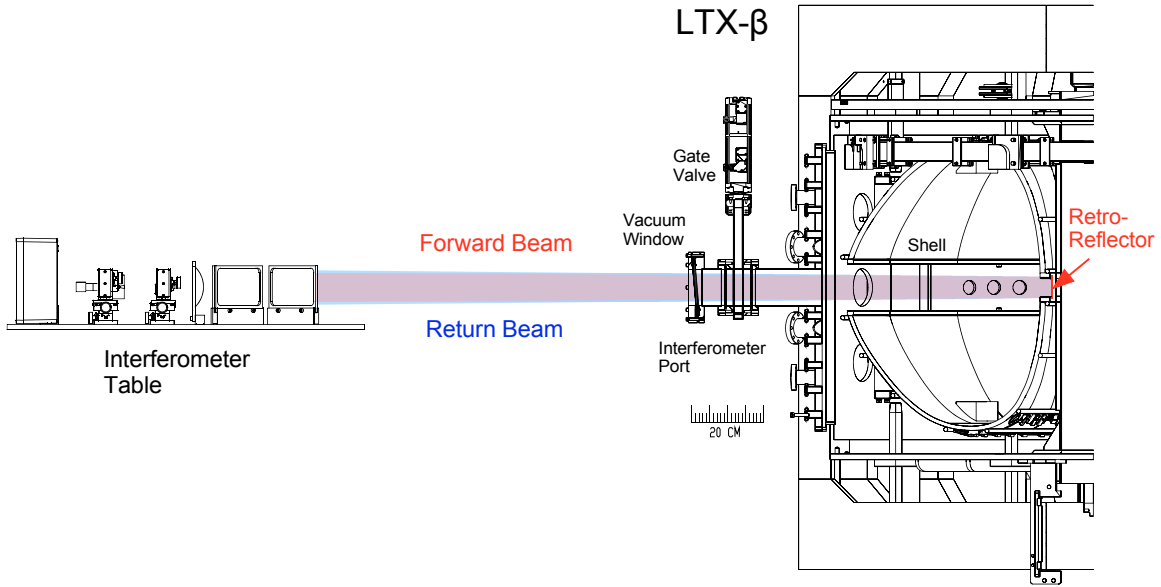
FIG. 1. Layout of the interferometer system, and its relative position to the LTX-β device.

forward scattering diagnostic.

II. DIAGNOSTIC AND MACHINE DESCRIPTION

LTX-β is a low-aspect ratio spherical torus, which retains the original dimensions of LTX (R_0=40 cm, a=26 cm). The upgraded machine will have auxiliary heating and core fueling via neutral beam injection (20 kV, 35 A). The vacuum vessel contains a close fitting shell on which lithium coatings are evaporated. Lithium wall coatings reduce wall recycling of hydrogen and lowers the edge neutral density. High electron temperatures with flat radial profiles have been predicted and observed on LTX.[2,4]

The optical layout for the $\lambda \approx 1$ mm interferometer is a Michelson type with a 2.5 inch square polished stainless steel mirror mounted to the centerstack as the retroreflector. This setup provides a single radial viewing chord through the poloidal shell gap at the midplane. Figure 1 shows the interferometer system relative to the LTX-β device. The plasma is accessed through a 6 inch diameter vacuum port, while the window (0.5 inch thick fused quartz) is tilted downward by 5° and has a $\sim$4 inch clear aperture.

The diagnostic technique for measuring the electron line density can be described as narrow-band chirped-frequency (or swept-wavelength) interferometry.[12] The source frequency $f(t)$ is swept in time as a linear sawtooth function around a center frequency f_0, with a period T [sweep rate γ=2f_Δ/T] and a maximum frequency deviation $f_\Delta \ll f_0$. The time delay between the probe and reference paths at the detector creates an IF signal, which can be described by

$$S_{\mathrm{IF}}(t) \propto \cos\left\{2\pi \frac{f_0}{c}\left[L_{\mathrm{opt}}(f_0) - c\tau_{\mathrm{g}}(f_0)\right] + 2\pi F t\right\}$$
$$\simeq \cos\left\{-2\pi \frac{f_0}{c}\frac{N_{\mathrm{L}}}{n_{\mathrm{c}}(f_0)} + 2\pi F t\right\}, \quad (1)$$

where c is the speed of light in vacuum, N_{L} is the electron line density, and the electron cutoff density $n_{\mathrm{c}}(f_0)$ is assumed to be much greater than the peak electron density in the plasma. The optical distance $L_{\mathrm{opt}}(f_0)$ and group delay $\tau_{\mathrm{g}}(f_0)$ are defined as integrals along the beam path through the plasma:

$$L_{\mathrm{opt}}(f_0) \equiv \int \mu(f_0, r)dr, \quad \tau_{\mathrm{g}}(f_0) \equiv \int \mu_{\mathrm{g}}(f_0, r)dr, \quad (2)$$

where $\mu(f_0, r)$ is the index of refraction and $\mu_{\mathrm{g}}(f_0, r)$ is the group index of refraction. The time dependence of $S_{\mathrm{IF}}(t)$ is set equal to the sawtooth period T=F^{-1} by using the condition $2f_\Delta$=$(\tau_{\mathrm{probe}} - \tau_{\mathrm{ref}})^{-1}$, where τ_{probe} and τ_{ref} are the time delays along the probe and reference paths, respectively. The path difference in vacuum for the system described here is 328 cm, which corresponds to $f_\Delta = 45.7$ MHz. At $f_0 = 288$ GHz, this results in a fractional change of 3×10^{-4} for the phase shift due to N_{L} over the range of the frequency sweep. $S_{\mathrm{IF}}(t)$ can deviate from a pure sinusoid at frequency F due to variations of the probe path during the plasma shot, as well as due to the tuning characteristics of the source and multiple passes of the beam through the arms of the interferometer. These effects can generate signal components at harmonics of F, which are reduced using a bandpass filter. The tuning voltage for the source frequency sweep provides a reference signal at frequency F, which is used to recover the phase change of the detector output due to the plasma. Swept-frequency interferometry utilizing hardware similar to that described below has been used on a number of plasma devices.[13,14]

Figure 2(a) shows the layout of the optical setup, while the block diagram in Fig. 2(b) includes the microwave and electronics components. The millimeter-wave source, consisting of a 96 GHz bias-tuned Gunn oscillator (Wise-Wave OVG-10960217-01) with an InP passive tripler, generates $\sim$10 mW of output at 288 GHz. A portion of the power is directed, using a 45 line-per-inch metal mesh beamsplitter ($\sim$15% reflection), along the reference path
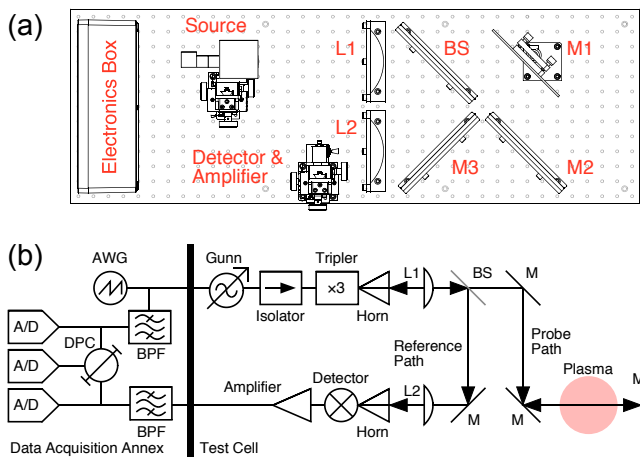
FIG. 2. (a) Top-down view of the interferometer table showing the location of of the optical components. (b) Block diagram of the interferometer layout and electronics. BPF: bandpass filter; L1, L2: lenses; M1, M2, M3: mirrors; BS: beam splitter; DPC: digital phase comparator; AWG: arbitrary waveform generator; A/D: analog to digital converter.
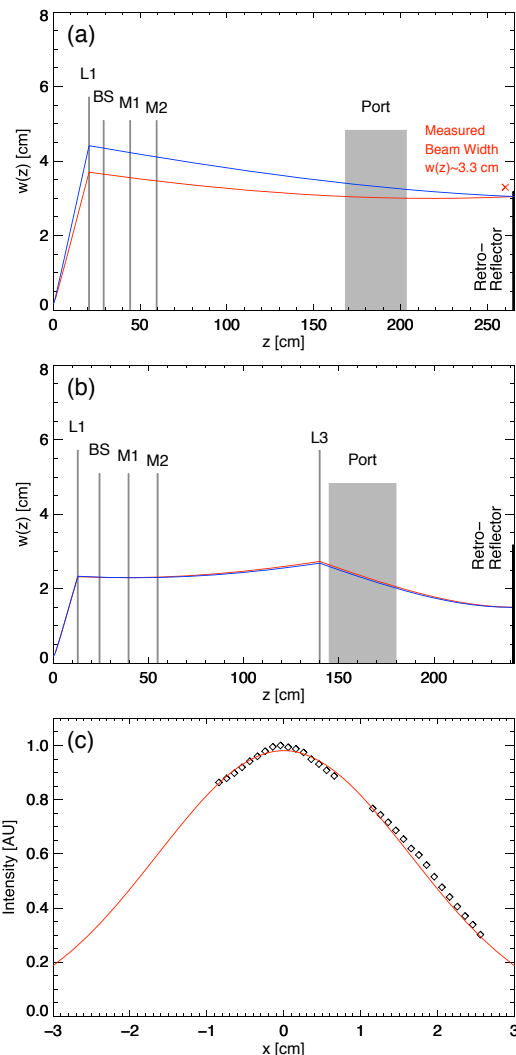

FIG. 3. (a) Calculated beam radius along the beam path. Forward propagating beam is shown in red, while the return beam from the retro-reflector is shown in blue. Also shown are the vertical dimensions of the components on the optical table and the retro-reflector, as well as the radius and extent of the interferometer port. The beam waist for the source antenna is located at the origin of the z-axis. (b) The same calculation for a beam that has been been optimized for FFS by introducing a second lens L3 (5 cm in front of the window) and reducing the distance between the optical table and the machine by $\sim$18.5 cm. The focal lengths for L1 and L3 are 13 cm and 104 cm, respectively. and the distance between the optical table and window has been reduced by $\sim$18.5 cm. (c) Measurement of the beam profile at the position $z = 260$ cm. The best fit to a Gaussian profile (red) gives a beam waist $w_z = 3.3$ cm [also indicated in (a)].

to the detector (Radiometer Physics WDT-325 waveguide detector) and video amplifier (gain: 150, bandwidth: 30 MHz) combination. The oscillator tuning voltage is provided by an arbitrary waveform generator (Agilent 33250A), which supplies an upward sawtooth voltage signal at a repetition rate of 750 kHz (nominal input IF for the digital phase comparator). Analog bandpass filter are used on both the reference signal (Krohn-Hite 3202R) and the IF signal (Krohn-Hite 3103) to generate sinusoidal inputs to the digital phase comparator. The filtered IF signal typically has a bandwidth of $0.5-1$ MHz and the final phase distortion is less than $3°$. These signals, as well as the phase comparator output, are sampled using a D-tAcq Solutions ACQ480ELF-8-LFP module housed in an ACQ1001Q carrier (up to 50 MSa/s sampling).

Both the source and detector are coupled to free space using Pickett-Potter type horns.[15] Lens L1 (spherical lens with focal length 20 cm) shown in Fig. 2(a) generates a weakly focused beam with a spot size of $\sim$3 cm (e^{-2} intensity radius) and a waist located at a distance of $\sim$135 cm from the interferometer table ($\sim$50 cm in front of the retro-reflector surface). The beam radius w is defined as the radius at which the intensity decreases to e^{-2} of its axial value, and the calculated beam size in vacuum as a function of the distance from the source (z-axis) is plotted in Fig. 3(a). The divergence angle of w is $\sim$0.6°. The return beam is focused back onto the launch horn, and the reflection from the tripler diode, collinear with the reference beam, is directed by the beamsplitter towards lens L2 (aspherical lens with focal length 6 cm) and the detector antenna. Figure 3(c) shows a measurement of the beam profile near the retro-reflector position [also indicated in Fig. 3(a)].

The optical layout shown in Figs. 2(a) and (b) utilizes only a single beamsplitter, while the conventional Michelson layout requires three. The probe and reference beams see no additional attenuating components before reaching the plasma and the detector, respectively. A larger probe wave is advantageous when competing with emissions from the plasma. The return beam passes through the beamsplitter twice before it is reflected by the tripler diode ($\sim$33 % reflection) and the same beamsplitter. The total attenuation of the return beam due to these components is approximately -27 dB.
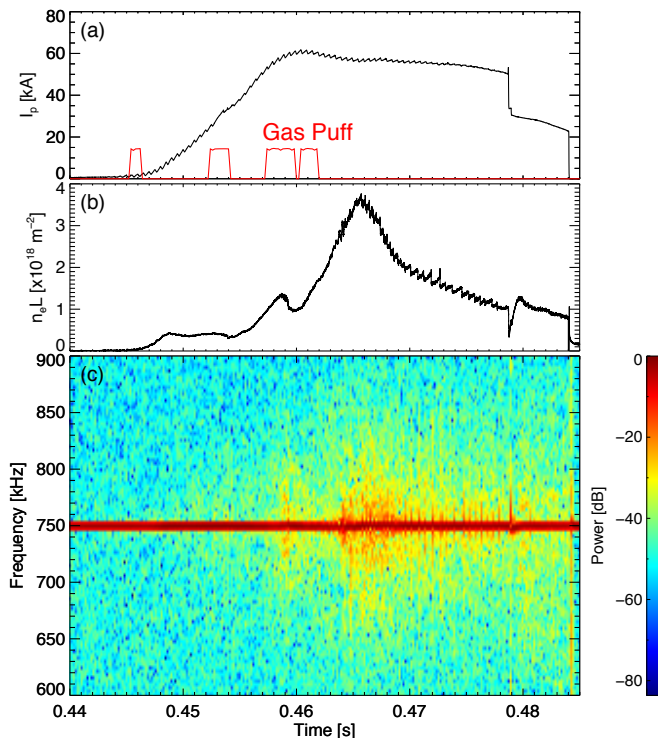
FIG. 4. Discharge parameters and interferometer signal spectra: (a) plasma current, (b) electron line density, and (c) spectrogram of the IF signal.

III. FAR-FORWARD SCATTERING FOR LTX-β

The interferometer hardware described above was originally designed for and installed on the National Spherical Torus Experiment (NSTX).[16] The equipment was subsequently moved to the LTX device, where the beam width of $\sim$3 cm at the retro-reflector location is comparable to the half-width of the retro-reflector [see Fig. 3(a)]. Truncation of the beam by an aperture with radius $A \leq 2.4w$ can significantly alter the beam profile due to diffraction effects.[17] For interferometry, this typically reduces the efficiency of the transmission line, where the effects are a loss of signal level and decreased signal-to-noise ratio. For FFS these effects may be severe, since changes to the beam profile can alter the $k_\perp$-response of the diagnostic and complicate quantitative interpretation of the data.

The optical setup can be modified to minimize beam truncation. Figure 3(b) shows an example of the proposed layout where beam propagation within the vacuum vessel has been tailored such that $A \sim 2w$ is satisfied at both the port entrance (window) and the retro-reflector surface. In addition, the optical table has been moved closer to the machine by $\sim$18.5 cm and lens L1 now has a focal length of 13 cm. A third lens L3 with a focal length of 104 cm has been introduced 5 cm from the vacuum window. We note that $A \geq 2.2w$ is now maintained for the remaining components on the optical table as well. Estimates of diffraction effects using a 3-D version of the FFT-based Beam Propagation Method (FFT-BPM)[18] show minimal variation of the beam profile for

these dimensions.

An important change due to a modification of the beam size is the increased sensitivity, for both interferometry and FFS, to higher $k_\perp$ fluctuations. The interferometer response $\exp(-k_\perp^2 w^2/4)$ has an e-folding point at $k_\perp w=2$, while the FFS response $k_\perp^2 w^2 \exp(-k_\perp^2 w^2/8)$ has a peak at $k_\perp w=2\sqrt{2}$ and e-folding points at $k_\perp w=1.13$ and 5.0. For the current beam path shown in Fig. 3(a), the forward and return beams have radii of $\sim$2.9 and $\sim$3.1 cm, respectively, at the midpoint of the outer radius [$z = 222.5$ cm in Fig. 3(a), where $R = R_0 + a/2$], while for the proposed layout in Fig. 3(b), both beams have a radius of $\sim$1.74 cm. Moving from the current layout to the proposed layout, these values correspond to a shift of the FFS response peak from $k_\perp$=0.95 cm^{-1} to 1.6 cm^{-1}, and a shift in the e-folding range from $k_\perp$=0.37−1.7 cm^{-1} to $k_\perp$=0.65−2.9 cm^{-1}. For interferometry, the corresponding shift in the e-folding point is from $k_\perp$=0.67 to 1.1 cm^{-1}. For FFS this also means better contrast since fluctuations close to $k_\perp \simeq 0$ will be more strongly filtered.

Finally, we note that all the of the calculations shown here were performed in 2-D using a flat vertical phase screen (Raman-Nath diffraction) to simulate the density perturbation and a Fourier optics approach[6] to calculate the propagation of the perturbed beam in vacuum. Scattering by plasma waves that obliquely intersect the probe beam and have a finite scattering volume has also been studied[7], however specific effects due to the curvature of the flux surfaces and up-down asymmetry due to a vertically shifted plasma require further study. In addition, the traditional FFS system will have the beam focused onto an array of detectors to generate a spatial profile of the beam intensity, while the setup described here focuses the entire beam onto a single receiving horn and detector. For a magnetized plasma, the actual beam will travel a 3-D path in space and effects such as beam refraction, beam drift,[20] and beam focusing or expansion, due to the transverse variation of the electron density, should be considered for realistic calculations. In addition, plasma perturbations will span a range of wavenumber values and occupy a 3-D volume. A future goal of this work is to apply existing beam propagation codes to address these issues; e.g., versions of the Beam Propagation Method,[18] beam tracing[19], and finite-difference time-domain.[21] Such studies will be required for quantitative analysis of the experimental data.

IV. MEASUREMENTS ON LTX

An example of experimental data from LTX using the interferometer hardware is shown in Fig. 4. Figures 4(a) and (b) show the plasma current I_p and the line density waveforms, respectively, for an Ohmic discharge. The working gas is H_2, and a large density rise is initiated by the gas puff at $t = 0.460$ s. Flat electron temperatures profiles with edge $T_e > 200$ eV (due to low recycling achieved by Li coating of the shell) are observed following the density peak in the latter portion of the discharge.[4]

Figure 4(c) shows a spectrogram of the raw interferometer IF signal. The signal spectrum is broad (compared to

the typical interferometry spectrum of a few tens of kHz), and rises in magnitude with the line density, indicating a dependence of the signal strength on the electron density. This is consistent with increased modulation of the IF signal due to a stronger scattered signal component. For chirped frequency operation, the detector output S_{IF} is proportional to $E_s E_{\mathrm{ref}} + E_p E_{\mathrm{ref}}$, where E_s, E_{ref}, and E_p are the electric fields due to FFS, the reference beam, and the probe beam, respectively The DC components, as well as the product $E_s E_p$, have been filtered with a bandpass filter centered at 750 kHz and having a bandwidth of 500 kHz. $E_s E_p$ is typically referred to as the homodyne FFS signal and is the quantity historically measured by FFS diagnostics. Operation of the system as an interferometer precludes measurement of the homodyne FFS signal, however simultaneous measurements on J-TEXT[11] of S_{IF} and the homodyne FFS signal have shown the spectral similarity of the two signals. The asymmetry in the spectrum of heterodyne interferometer signals has long been attributed to asymmetries in the distribution of the density fluctuations across the probe beam. In addition, detection of the full homodyne FFS spectrum requires measurement of the DC portion of the signal, where instrumental and pickup noise can be an issue. The determination of a fluctuation level requires knowledge of the probe beam intensity, which is already available from S_{IF}. The extraction of useful information about E_s from S_{IF} is a topic of ongoing research.

Finally, in some LTX discharges the radial structure and rotation of a coherent MHD mode can be determined from the electron density profiles provided by the FM-CW reflectometer. This data can serve as a test case for developing a reliable synthetic diagnostic for FFS.

V. SUMMARY AND FUTURE WORK

This article documents the diagnostic hardware and operation principle of the $\lambda \approx 1$ mm interferometer for the LTX-β device. Chirped-frequency interferometry allows the system to use a single swept-frequency source and detector to generate the heterodyne signal. An example of interferometry results from the LTX device, as well as evidence of FFS, is presented. The $k_\perp$ sensitivity of the system to FFS is evaluated using the phase screen model with Fourier optics, and an improved optical layout is presented for enhancing these measurements.

Future work will involve implementing these hardware changes, as well as developing additional analytic models and synthetic diagnostic codes for better quantitative analysis of the experimental data.

[1]R. Majeski, L. Berzak, T. Gray, R. Kaita, T. Kozub, F. Levinton, D. P. Lundberg, J. Manickam, G. V. Pereverzev, K. Snieckus, V. Soukhanovskii, J. Spaleta, D. Stotler, T. Strickler, J. Timberlake, J. Yoo and L. Zakharov, Nucl. Fusion **49**, 055014 (2009).

[2]R. Majeski, R. E. Bell, D. P. Boyle, R. Kaita, T. Kozub, B. P. LeBlanc, M. Lucia, R. Maingi, E. Merino, Y. Raitses, J. C. Schmitt J. P. Allain, F. Bedoya, J. Bialek, T. M. Biewer, J. M. Canik, L. Buzi, B. E. Koel, M. I. Patino, A. M. Capece, C. Hansen, T. Jarboe, S. Kubota8, W. A. Peebles, K. Tritz, Phys. Plasmas **24**, 056110 (2017).

[3]S. Kubota, R. Majeski, W. A. Peebles, R. E. Bell, D. P. Boyle, R. Kaita, T. Kozub, M. Lucia, E. Merino, X. V. Nguyen, T. L. Rhodes, J. C. Schmitt, Rev. Sci. Instrum. **88**, 053502 (2017).

[4]D. P. Boyle, R. Majeski, J. C. Schmitt, C. Hansen, R. Kaita, S. Kubota, M. Lucia, T. D. Rognlien, Phys. Rev. Lett. **119**, 015001 (2017).

[5]R. E. Slusher, C. M. Surko, Physics Fluids **23**, 472.

[6]D. E. Evans, M. von Hellerman, E. Holzhauer, Plasma Physics **24**, 819 (1982).

[7]Y. Sonoda, Y. Suetsugu, K. Muraoka, M. Akazaki, Plasma Physics **25**, 1113 (1983).

[8]C. B. Deng, D. L. Brower, Rev. Sci. Instrum. textbf81, 10D503 (2010).

[9]W. X. Ding, L. Lin, J. R. Duff, D. L. Brower, J. S. Sarff, Rev. Sci. Instrum. **83**, 10E302 (2012).

[10]B. H. Deng, J. S. Kinley, K. Knapp, P. Feng, R. Martinez, C. Weixel, S. Armstrong, R. Hayashi, A. Longman, R. Mendoza, H. Gota, M. Tuszewski, Rev. Sci. Instrum. **85**, 11D401 (2014).

[11]P. Shi, J. Chen, L. Gao, Y. Liu, H. Liu, Y. N. Zhou, G. Zhuang, Rev. Sci. Instrum. **87**, 11E110 (2016).

[12]E. D. Moore, "Advances in Swept-Wavelength Interferometry for Precision Measurements", Ph. D. Thesis, University of Colorado, 2011.

[13]L. Porte, C. L. Rettig, W. A. Peebles, and X. Nguyen, Rev. Sci. Instrum. **70**, 1064 (1082).

[14]D. L. Brower, C. Deng, W. X. Ding, D. T. Anderson and W. Mason, Rev. Sci. Instrum. **72**, 1081 (2001).

[15]H. M. Pickett, J. C. Hardy, J. Farhoomand, IEEE T. Microw. Theory, Vol. MTT-32, No. 8, 936 (1984).

[16]M. Ono *et al.*, Nucl. Fusion **40**, 557 (2000).

[17]G. A. Ediss, IEEE Proceedings H, Volume 137, Issue 3, 171 (1990).

[18]O. K. Erskoy, *Diffraction, Fourier Optics and Imaging*, Wiley-Interscience (2006).

[19]G. V. Pereverzev, Phys. Plasmas **5**, 3529 (1998).

[20]P.-A. Gourdain, W. A. Peebles, Plasma Phys. Control. Fusion **50**, 025004 (2008).

[21]A. Taflove, S. C. Hagness, *Computational Electrodynamics: The Finite-Difference Time-Domain Method, 3e*, Artech House (2005).

LTX-β

Gate Valve

Vacuum Window

Forward Beam

Return Beam

Interferometer Port

Interferometer Table

Shell

Retro-Reflector

20 CM

(a)

Electronics Box

Source

L1

BS

M1

L2

Detector & Amplifier

M3

M2

(b)

AWG

A/D

DPC

A/D

A/D

BPF

BPF

Data Acquisition Annex

Test Cell

Gunn

Isolator

Tripler
×3

Horn

L1

Reference Path

BS

M

Probe Path

M

Amplifier

Detector

Horn

L2

M

M

Plasma

M

(a) L1 BS M1 M2 Port — Measured Beam Width w(z)~3.3 cm — Retro-Reflector

(b) L1 BS M1 M2 L3 Port — Retro-Reflector

(c)